

# Daily global methane super-emitter detection and source identification with sub-daily tracking

Tobias A. de Jong<sup>1,\*</sup>, Joannes D. Maasakkers<sup>1</sup>, Itziar Irakulis-Loitxate<sup>2,3</sup>,  
Cynthia A. Randles<sup>2</sup>, Paul Tol<sup>1</sup>, Ilse Aben<sup>1,4</sup>

<sup>1</sup> SRON Netherlands Institute for Space Research, Leiden, The Netherlands

<sup>2</sup> International Methane Emission Observatory, United Nations Environment Program, Paris, France

<sup>3</sup> Research Institute of Water and Environmental Engineering (IIAMA),  
Universitat Politècnica de València (UPV), Valencia, Spain

<sup>4</sup> Department of Earth Sciences, Vrije Universiteit Amsterdam, Amsterdam, The Netherlands

\* t.a.de.jong@sron.nl

January 31, 2024

This is a non-peer reviewed preprint submitted to EarthArXiv, submitted to peer review at Geophysical Research Letters.

## Abstract

We use the Shortwave Infrared bands of the Visible Infrared Imaging Radiometer Suite (VIIRS) satellite instruments to retrieve atmospheric methane enhancements with 750 m resolution. We show that the three VIIRS instruments in orbit uniquely enhance the currently-employed capabilities of tracking methane super-emission events. The VIIRS instrument on Suomi-NPP and the TROPOMI instrument on Sentinel-5 Precursor have overpasses that are only a few minutes apart, which allows for direct identification of methane super-emitter sources by VIIRS as first detected by TROPOMI. The co-location also allows us to cross-validate our VIIRS methane enhancements with TROPOMI. Furthermore, we show how the global multiple overpasses per day by VIIRS and Sentinel-3 give a unique insight in the timeline of emissions and can be vital in understanding and attributing transient emissions.

## Key Points

- Methane super-emitter localization at 0.75km resolution using VIIRS including concurrently with TROPOMI super-emitter detection.
- Cross-validation of multi-band multi-pass method by comparison of co-located TROPOMI and Suomi-NPP VIIRS measurements.
- At least 4 times per day global coverage by combining three VIIRS instruments with Sentinel-3 SLSTR data.

## 1 Introduction

Methane is a potent greenhouse gas, and curbing the emission of methane is vital to limiting global warming in the near future [1, 2]. A relatively large part of the global anthropogenic methane emission comes from a small number of so-called super-emitters, emitting large amounts of methane from point sources. A key target for mitigation are super-emitters from oil and gas infrastructure, which might emit as part of routine operation procedure, due to aging, faulty and leaky equipment, or as needed for safety procedures [3]. The TROPOMI satellite instrument aboard Sentinel-5P provides daily, high-precision coverage of atmospheric methane, at a resolution of  $5.5 \times 7$  kilometers [4, 5]. To pinpoint sources to individual facilities and enable mitigation, higher resolution is needed. Furthermore, a single daily overpass is insufficient to detect and locate all transient events. To both these ends, it has been shown that in addition to methane-specific instruments such as GHGSat and targeted hyperspectral imagers [6], several band imagers (including Sentinel 2 and 3), while not designed for it, can be used to visualize large methane enhancements under favorable conditions [7–9]. Although retrieved methane quantities are less accurate due to the lack of spectral resolution, the 20m-500m spatial resolution of these satellite instruments enables the identification of sources. Here, we report on methane retrieval using the Visible Infrared Imaging Radiometer Suite (VIIRS).

The VIIRS instruments are on board the satellites of the Joint Polar Satellite System (JPSS), consisting of Suomi-NPP, JPSS-1 (after launch also known as NOAA-20) and, since 27 February 2023, JPSS-2 (NOAA-21), orbiting in sun-synchronous polar orbits with equatorial crossing times within about an hour of 1:30 PM. The VIIRS instruments have 5 imaging spectral bands with a nominal resolution of 375 m and 16 moderate resolution bands with a nominal resolution of 750 m, which include the the Shortwave Infrared (SWIR) bands (M10 and M11) used for methane retrieval in this work. This spatial resolution is coarser than the other aforementioned band imagers, but still much higher than TROPOMI’s spatial resolution. VIIRS’ swath width of 3000km (somewhat wider than TROPOMI’s) enables global coverage by each instrument within a day, resulting in three or more separate overpasses every day for any location on Earth while all three satellites are active.

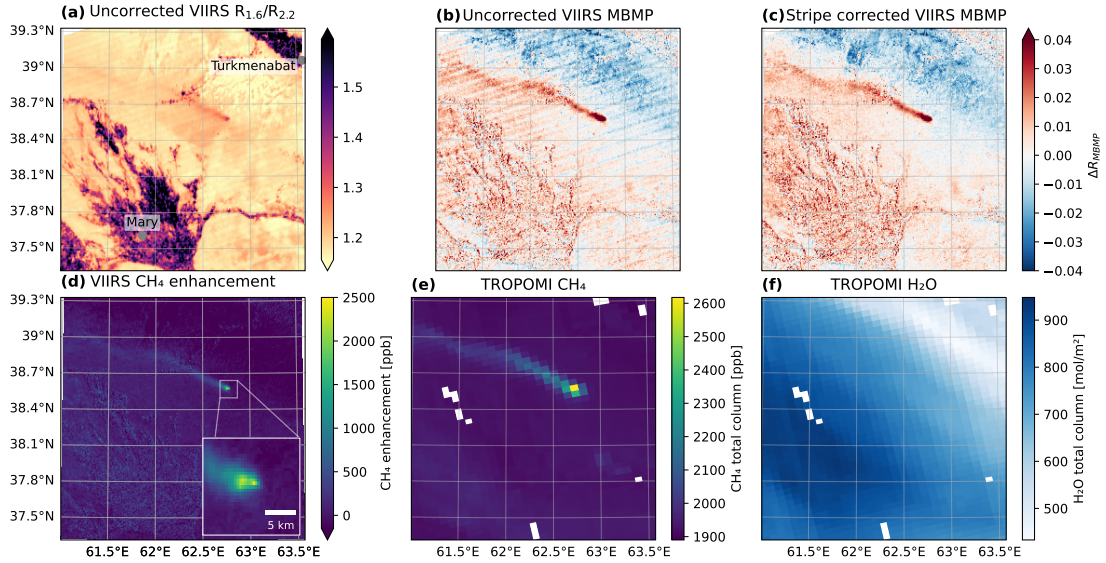


Figure 1: (a) VIIRS Band ratio using bands M10 and M11 for the Suomi-NPP overpass of the compressor station ( $38.569^{\circ}\text{N}$ ,  $62.788^{\circ}\text{E}$ , at the Malay oil field, Turkmenistan) showing methane emissions on October 2<sup>nd</sup> 2023 (08:55 UTC). (b) Uncorrected VIIRS MBMP signal. (c) Same as (b), but corrected for stripes due to detector differences. (d)  $\text{CH}_4$  enhancements retrieved from (c). (e) TROPOMI methane total columns from the overpass on the same day (08:59 UTC). (f) TROPOMI water total column of the same overpass.

A unique feature of Suomi-NPP VIIRS is the co-location within 5 minutes with TROPOMI observations. We will show that this allows direct identification for the largest methane super-emitters detected with TROPOMI [10], and cross-validation of methane enhancements between VIIRS and TROPOMI.

## 2 Methods

We retrieve total column methane enhancements from SWIR reflectance in the  $1.6\ \mu\text{m}$  and  $2.2\ \mu\text{m}$  bands by adapting the methods introduced in Varon et al. [7]. The MBMP method uses the reflectances in a reference band ( $1.6\ \mu\text{m}$ ) and on a reference day to remove any non-methane signals from the  $2.2\ \mu\text{m}$  band on the observation day. The signal  $\Delta R_{\text{MBMP}}$  is calculated by subtracting the reference scene composed of the median of similar scenes and taking the difference between the two bands. Assuming the reference day is enhancement-free, this corresponds to the following:

$$\Delta R_{\text{MBMP}} = \frac{c_{2.2}R_{2.2}}{R'_{2.2}} - \frac{c_{1.6}R_{1.6}}{R'_{1.6}}$$

where the constants  $c_i$  are the ratios of the median values of the band radiances on the reference day  $R'_i$  and on the measurements day  $R_i$  for the band with wavelength  $i\ \mu\text{m}$ . To obtain methane concentrations,  $\Delta R_{\text{MBMP}}$  is compared to a radiative transfer simulation.

### 2.1 Data processing

Both the VIIRS (aboard JPSS) and the Sea and Land Surface Temperature Radiometer (SLSTR, aboard Sentinel-3) instruments consist of a row of detectors (16 for VIIRS,  $2 \times 4$  for SLSTR. For SLSTR, only data of the 4 detectors of the so-called a-grid are used in this work), swiped across the swath by a rotating mirror. Although the detectors are regularly calibrated in-orbit and the stripes are not dominant in a direct band ratio (Figure 1(a) shows an example), the  $\Delta R_{\text{MBMP}}$  shows stripes corresponding to the different detectors (Figure 1(b)). These stripes are most likely

caused by the slight differences in the detectors’ spectral response (See Supplemental Figure S2). To correct the stripes, we fit an effective, per-detector, offset and gain for each  $\sim 100 \times 100\text{km}^2$  VIIRS scene (for each overpass separately). We do this by minimizing the difference in radiance between geospatially neighboring pixels for each band, while keeping the overall gain and offset constant. For SLSTR, we additionally include the typically redundant ‘orphan pixels’ (which are excluded from the square grid of the level-1b product) to optimize coverage of small scale features [11].

After stripe correction, we resample all clear-sky overpasses within a window of typically 16 days to a common 500 m grid by cubic interpolation. We then normalize the pixels of each individual band and overpass by dividing by the median radiance value, and then compute  $\Delta R_{\text{MBMP}}$  (Figure 1(c)). To minimize the error introduced in the MBMP, we compose the reference measurement out of up to ten different (VIIRS or Sentinel-3) overpasses that best match the viewing angles and solar angles of the observation measurement. We find this significantly improves the signal, as these angles have a significant influence on the radiation absorbed in terms of the effective optical depth of the atmosphere via the air mass factor (AMF), but also in terms of the reflectance of the surface, often described with a Bidirectional Reflectance Distribution function (BRDF) [12, 13].

## 2.2 Radiative transfer simulation

Similar to earlier work [7], we compare the measured radiance difference to a 25-layer clear-sky radiative transfer simulation:

$$m(\Delta\Omega) = \frac{T_{2.2}(\Omega + \Delta\Omega)}{T_{2.2}(\Omega)} - \frac{T_{1.6}(\Omega + \Delta\Omega)}{T_{1.6}(\Omega)}$$

Where  $T_{1.6}(\Omega)$  and  $T_{2.2}(\Omega)$  are the calculated transmittances for a methane column concentration  $\Omega$  in the 1.6  $\mu\text{m}$  and 2.2  $\mu\text{m}$  band respectively. The methane enhancement  $\Delta\Omega$  is added in the lowest 1km-thick layer of the model atmosphere. The methane enhancement is retrieved by interpolating a lookup table of signal levels for given concentrations and AMF values pre-computed using this simulation. The result is shown in Figure 1(d). The sensitivity of each instrument to radiation varies as a function of wavelength, even within a band. This variation is described by the instrument-specific Spectral Response Functions (SRF, See Supplemental Figure S1). We account for these sensitivities in the simulations by integrating the product of the sun emission spectrum, the absorption lines, and the SRF over the bandwidth of both bands. To be able to put the methane sensitivity of VIIRS in context, we also do this for other band imagers [7, 14, 15]. We use the US standard atmosphere [16], but scale the  $\text{CH}_4$ ,  $\text{CO}_2$  and  $\text{N}_2\text{O}$  concentrations to 2023 values of 1894 ppb, 416.7 ppm, and 334 ppb respectively [17, 18]. This shifts the retrieved methane enhancements up by around 5% because of the non-linear methane sensitivity (Supplement Figure S1c).

## 2.3 Plume masking and uncertainty estimates

To create a plume mask, we use the fact that the methane plume is an outlier compared to the normal spread in values. We therefore compute an outlier-robust statistical metric of the spread, the median absolute deviation (MAD), for each geolocated pixel in the resampled dataset of multiple overpasses. Assuming normally distributed values, the MAD is approximately 1.5 times the standard deviation. We divide the signal in each pixel by the MAD, smoothing the resulting values with a 2D Gaussian filter with a width of  $\sigma = 2$  pixels, and selecting only pixels that lie more than 1.2-3.0 standard deviations above the median value. The threshold is optimized for each specific case based on visual inspection. Additionally, this gives a per-pixel uncertainty of the retrieved methane signal, by comparing with retrieved values of a signal shifted by plus and minus one standard deviation.

## 3 Results

### 3.1 VIIRS sensitivity analysis

The retrieved VIIRS methane enhancement for the Malay compressor station plume (Figure 1(d)), shows a clear correlation with TROPOMI methane (Figure 1(e)), giving confidence in the VIIRS-retrieved methane. We do find a significant sensitivity to water vapor, as visible from the correlation of the TROPOMI H<sub>2</sub>O total column in Figure 1(f) and the VIIRS signal in Figure 1(c) (See also Supplementary Figure S3). The water vapor patterns are at a coarser spatial scale than the retrieved methane plumes. Therefore, although they influence the retrieved methane enhancements, they do not affect our ability to detect methane plumes using VIIRS. The sensitivity to water is to be expected, as water has absorption lines in the used SWIR bands. Fully accounting for the water sensitivity would require accounting for the continuum background of the water spectrum [19].

To compare the methane sensitivity of all methane-sensitive band imagers, we use radiative transfer simulations to calculate the signal due to methane enhancements (Supplementary Figure S1). The VIIRS and SLSTR [9] instruments are more sensitive to CH<sub>4</sub> than the Landsat and Sentinel-2 band imagers. This results in plumes being visible over much larger spatial scales for VIIRS/SLSTR compared to Landsat/Sentinel-2. However, for detection of emission plumes, this is partially compensated by the much higher spatial resolutions of the land imagers, which gives them much larger (more concentrated) methane concentration enhancements per pixel near source locations.

### 3.2 Plume visualization

To illustrate the ability of VIIRS to measure methane enhancements, we look at the full time series of a 3-day emission event at a compressor station in Malay, Eastern Turkmenistan in a desert region with favorable observation conditions, which started on October 1st 2023. During this event, there were only 3 clear-sky overpasses of TROPOMI and 1 overpass of Sentinel-2. In contrast, there were 3 overpasses of Sentinel-3 satellites and 9 overpasses of JPSS satellites. The Sentinel-3 and JPSS overpasses are visualized in Figure 2, together with the corresponding TROPOMI overpasses in insets. Comparing VIIRS and SLSTR, we find from the MAD a distribution of per-pixel errors with a mean of 118ppb and a standard deviation of 52 ppb for VIIRS. For the SLSTR data, we find a mean error of 204 ppb and a standard deviation of the error of 104ppb. Here, it is clear that combining multiple overpasses a day yields additional insight. In particular, the turning of the wind and subsequent backfolding of the plume over the source is clear on October 1. This effect would skew any quantification of the emission rate if not properly accounted for. For October 2, dispersion of the plume is visible as the atmosphere gets more turbulent during the morning.

### 3.3 Cross-validation with TROPOMI

Suomi-NPP is in the same orbit as Sentinel-5P, with a difference in overpass time of only 4 minutes. This provides not only a unique opportunity for concurrent identification of facilities responsible for TROPOMI-detected methane plumes, but also for cross-validation. While the MAD gives an estimate of the random error for MBMP methods, we should also assess any systematic errors which are much harder to extract from statistics alone. We therefore cross-validate our methane enhancements retrieved using MBMP methods against well-established methane enhancements measured by TROPOMI, which itself are validated against TCCON [21].

To directly compare co-located VIIRS and TROPOMI methane measurements, we resample the VIIRS radiances of all overpasses in a dataset to the exact TROPOMI pixels of the co-located overpasses. We then compute the MBMP methane enhancement and the MAD across the footprint of each TROPOMI pixel. We compare these methane enhancements with TROPOMI data, as shown in Figure 2(m-o). Linear fits of the plume data show good agreement between

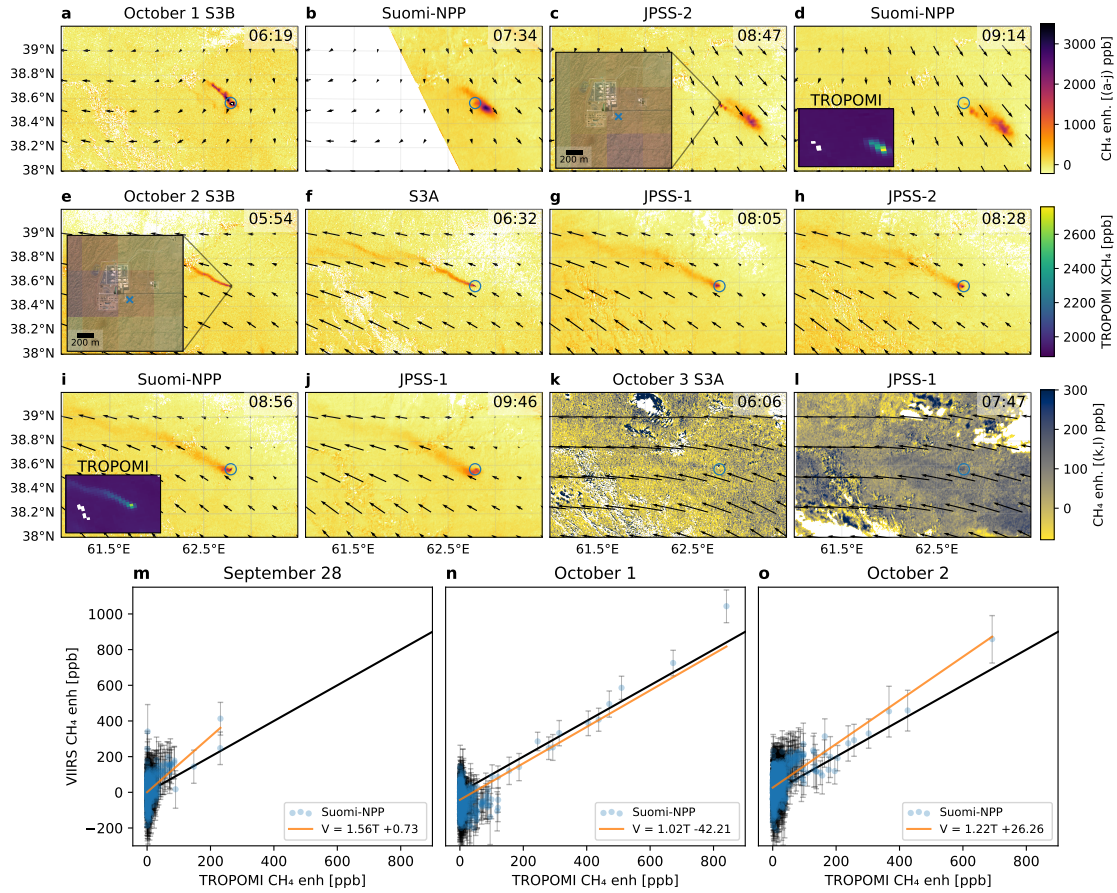


Figure 2: Retrieved VIIRS and Sentinel-3 SLTR methane enhancements for a 2023 compressor station emission event in the Malay oil field, Eastern Turkmenistan. Enhancements on October 3 are shown on a different color scale, as they are much smaller. In all subplots, ERA5 100m winds are shown as arrows corresponding to 1 hour travel distance. Insets in (c,e) show the base of the plume overlaid over ESRI world imagery of the compressor station [20]. Blue  $\times$ 's mark the Sentinel-2 derived most likely origin of the emission. Insets in (d,i) show the TROPOMI data from corresponding overpasses at 9:18 UTC and 9:00 UTC respectively, where (i) corresponds to the same overpass as Figure 1. (All TROPOMI insets in this work show the same field of view as the main panel.) (m-o) Pixel-by-pixel comparison of the VIIRS and TROPOMI enhancements. A best linear fit is shown in orange, with the one-to-one line in black. ((n,o) corresponds to (d, i), see also Supplementary Figure S4)

TROPOMI and MBMP data (slopes of 1.02-1.56), although the VIIRS data seems to slightly overestimate the enhancements relative to TROPOMI. More generally, we find that the agreement between VIIRS and TROPOMI seems to vary from case to case, confirming the accuracy of the VIIRS retrieval is worse than TROPOMI, even under these near-optimal observing conditions. Nevertheless, this serves as the first direct validation of enhancements obtained with the MBMP methane retrieval method.

As part of TROPOMI's methane retrieval, the total water column, aerosol optical depth (AOD) and CO concentration are retrieved simultaneously. Comparing these with resampled VIIRS MBMP data, the only significant correlation we find is with the background water column ( $\sim 4 \times 10^{-5}$  per mol  $\text{H}_2\text{O} / \text{m}^2$ ), as expected based on Figure 1 (See Supplementary Figure S3). We find the same dependency to within uncertainty by comparing the Sentinel-3 SLSTR MBMP signal with the Sentinel-3 OLCI-derived Integrated Water Vapour column product [22].

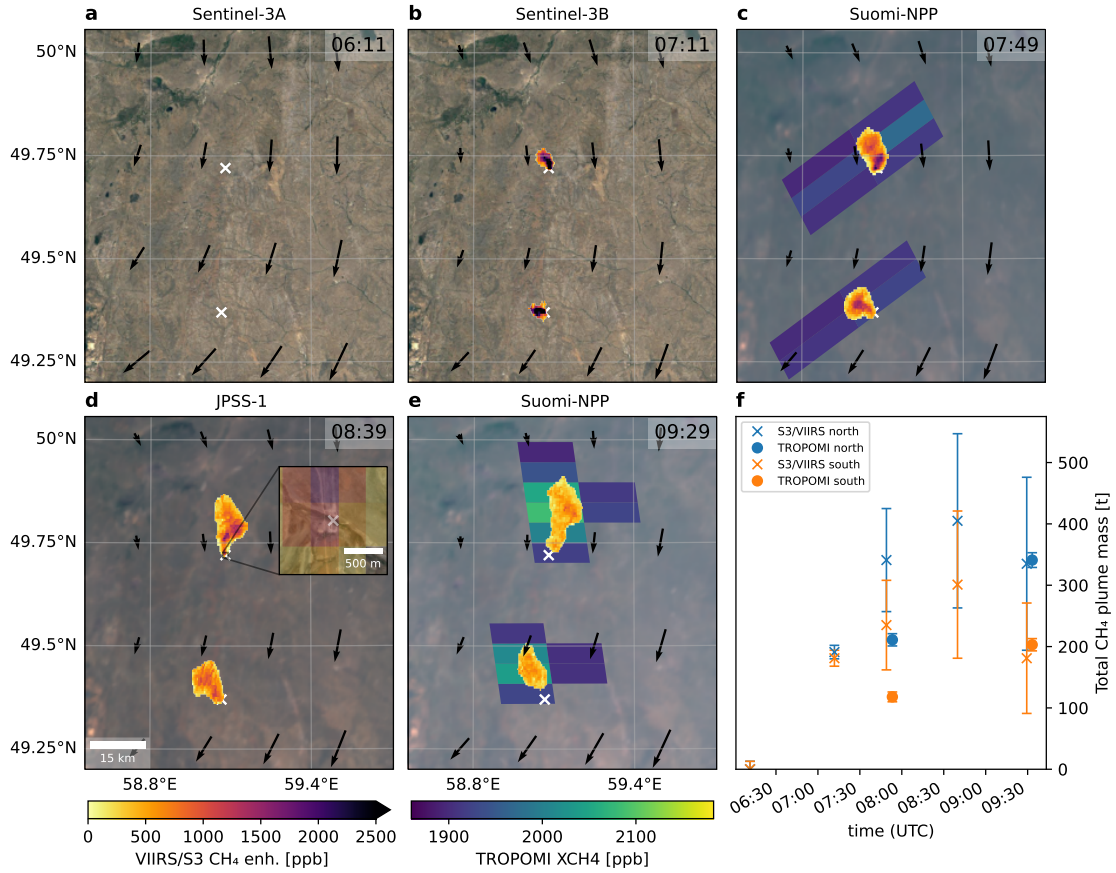


Figure 3: Gas release at two gas pipeline block valve stations in Kazakhstan on May 14, 2021, the same event as studied in Schuit et al. with TROPOMI and Sentinel-2 [10]. (a) Sentinel-3A overpass before emissions started. (b) Sentinel-3B overpass after the start of emissions (background (a) and (b) Google Maps imagery [23]). (c-e) JPSS overpasses. For the Suomi-NPP overpasses, the corresponding TROPOMI pixels of the plume, from overpasses at 7:53 and 9:33 respectively, are also shown. Background images are VIIRS level-1-derived RGB images of the respective overpasses. (inset d) Zoom of the northern source of the northern plume overlaid over a Google maps background [23]. The gas pipeline can be distinguished running from North to South. (f) Timeline of the total plume mass estimates. Arrows in (a-e) correspond to the 100m ERA5 wind, interpolated to the time of overpass, with arrow length corresponding to the displacement during 1 hour.

In addition, we can directly compare the TROPOMI pixels to the native-resolution VIIRS data in terms of total mass enhancement in a plume. This comparison is particularly useful for transient emissions, which result in a well-defined plume drifting away from the source with a constant total methane mass imaged in multiple overpasses. In Figure 3, we show such a comparison for a gas release event at two block valve stations in Kazakhstan. The emissions started sometime after the overpass of Sentinel-3A at 6AM UTC, but before the overpass of Sentinel-3B at 7AM (Figure 3(a,b)). There are two separate TROPOMI overpasses from consecutive orbits covering this event (Figure 3(c,e)), where the emission had ceased for the latter overpass, as the VIIRS data shows that the plumes have detached from the source by a few kilometers. An additional VIIRS overpass was made by JPSS-1 in between the TROPOMI observations (Figure 3(d)). The estimates for the total methane mass in the plume match between VIIRS and TROPOMI to within the uncertainty for the later overpass, but VIIRS plume mass estimates are significantly higher than TROPOMI in the first co-located overpass (Figure 3(f)). We attribute this to the just-emitted plume being very concentrated within a small part of the TROPOMI

pixels, leading to an underestimation of the plume mass when the incoming radiation is averaged over the entire pixel, the so-called partial pixel enhancement effect [14].

The multiple overpasses also allow us to evaluate the ERA5 reanalysis wind [24]. The observed high-resolution plumes clearly show that the wind is blowing the plume in northward direction, which contradicts the wind from ERA5, as indicated by the arrows, which is southward. Errors in wind speed and direction can thus be estimated, aiding source identification and the interpretation of the TROPOMI observations.

### 3.4 Applications of combining VIIRS and TROPOMI methane observations

We apply the VIIRS retrieval to zoom-in on several plumes detected with TROPOMI a variety of sources from the oil and gas sector worldwide (Figure 4). Although detection limits are best over bright, uniform, desert-like areas, such as a production facility in Algeria and a compressor station in Kazakhstan (Figure 4(b,c)), we show that retrieval can also work over less ideal scenes such as a mountainous area in the northwestern US, Siberian forest, and agricultural land in Argentina (Figure 4(a,d,e)), provided the enhancements are large enough.

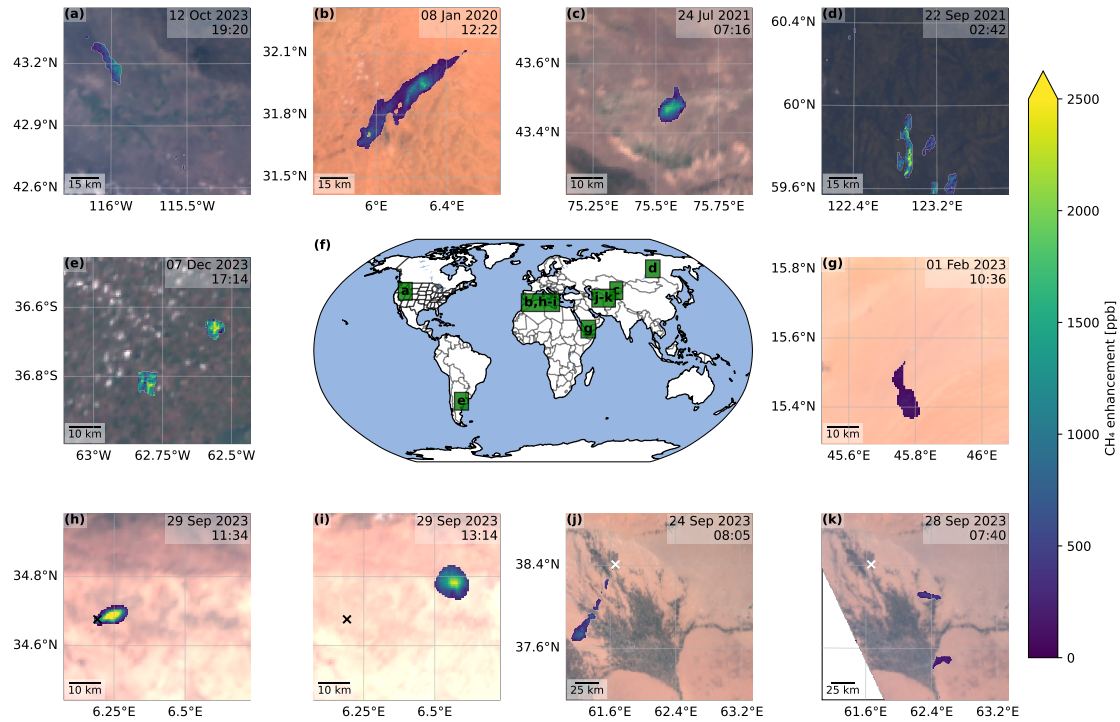


Figure 4: Examples of VIIRS detected plumes. (a) Plume from a gas line explosion in Middleton, Idaho (USA) [25]. (b) Plume near the Hassi Messaoud oil production field, Algeria [9]. (c) Gas compressor station in Eastern Kazakhstan. (d) Gas infrastructure in Northern Siberia. (e) Two plumes, likely from two block valves releasing near the Saturno gas compressor station in Argentina. (f) World map marking the locations of the plumes. (g) Oil/Gas infrastructure in Yemen. (h,i) Gas compressor station release in Algeria. The source is marked by a black cross. (j,k) Plumes in the Mary region of Turkmenistan, traced back to an oil and gas facility located  $38.41^{\circ}\text{N}$ ,  $61.66^{\circ}\text{E}$  (marked with a white cross). Full time series with ERA5 winds and corresponding TROPOMI data for all cases are shown in Supplementary Figures S5-S12. All background images are RGB images from the corresponding VIIRS overpass.

For all these examples, VIIRS provides more clarity on the source after a methane signal

was first detected with TROPOMI. In cases where multiple potential emitters are nearby, VIIRS cannot give the same level of detail as instruments with a spatial resolution of  $\sim 25\text{m}$ , but it was able to point out a source facility for all of these plumes. The plume shown in Figure 4(g), over a gas facility in the desert of Yemen, highlights the sensitivity of VIIRS in a near best-case scenario: The plume can be detected and masked, while the maximum methane enhancement in the plume is less than 230 ppb.

As TROPOMI can only detect clear-sky plumes, VIIRS will inherently have cloud-free coverage of the same plumes for at least the co-located Suomi-NPP overpass, while vice-versa the TROPOMI overpass verifies that the observed signal in the VIIRS data indeed corresponds to a methane plume. An example is shown in Figure 4(i), a methane release on 29 Sept. 2023 from a compressor station in northeastern Algeria, first detected by TROPOMI. This is a strong short-duration plume typically associated with the oil and gas sector, where the emission has already ceased and the plume is detached from the source. VIIRS is especially useful in such cases, because prior VIIRS/Sentinel-3 overpasses can be used to find the source. In this case, we can directly attribute it to a facility 40km upwind of the TROPOMI detection (Figure 4(h)). The temporal information provided by the VIIRS and Sentinel-3 retrievals can also be vital in understanding the emission event when winds are complicated. This is highlighted by the multiple overpasses in a single day is shown in Figure 4(j,k) (Full time series in Supplementary Figure S9). In this case, three plumes were detected with TROPOMI in eastern Turkmenistan at the end of September 2023. Purely based on the individual TROPOMI overpasses, the plumes appear more than 80km apart and can not be (confidently) attributed to a single source because of complicated wind patterns. However, using the additional JPSS and Sentinel-3 overpasses, we can trace all three TROPOMI detections back through time to the same oil and gas facility.

## 4 Conclusion and Outlook

We have shown that under favorable conditions, the VIIRS instruments aboard the JPSS satellites can be used to detect and image super-emitter methane plumes, similar to other band imagers. This is a unique addition to the rapidly expanding suite of satellite instruments able to observe methane super-emitters, for three reasons. First, the co-location within a few minutes of the Suomi-NPP VIIRS instrument with TROPOMI means that for every methane plume detected with TROPOMI, a higher resolution VIIRS dataset of the same plume is available, which helps to identify the emission source. Second, for each event, one to four additional VIIRS observations are available through the complete JPSS constellation at intervals of 25 or 50 minutes. This gives significant insight in the temporal evolution of emissions, in particular for transient emissions. Using TROPOMI, VIIRS and SLSTR together to monitor emissions thus gives a much more complete picture. Third, the co-location of Suomi-NPP with TROPOMI allows for direct cross-validation of methane enhancements obtained using MBMP methods with enhancements obtained with TROPOMI. This enables identification of error sources of MBMP methods. In particular, we have shown that water vapor has a strong influence on the methane retrieved using MBMP methods. Although this does not prevent localization, a method directly correcting for water vapor would improve improvement quantification accuracy. For Sentinel-3, a direct input for that is available in the form of the IWV product that is based on the OLCI bands. For VIIRS, there is no direct water vapor product available. Although its M11-M16 bands do have some water vapor sensitivity, they are not suited for correction using a linear model.

Looking to the future, everything described here will also be applicable to the methane measurements of Sentinel-5 and the VIIRS-like METimage, both aboard the Metop-SG-A satellite. DLR's METimage has a spatial resolution of 500m and has bands around 900 nm that could be used to correct for water vapor [26]. All current and future band imagers can build on the cross-validation between TROPOMI and VIIRS. Nevertheless, high-precision spectral imagers are needed to accurately assess and remedy the emissions of smaller sources and additional instruments are needed to fill the gap in temporal coverage in the local afternoon. Combining

all these instruments with different overpass times within the framework presented here greatly enhances the completeness of our ability to monitor methane super-emitters around the world.

## Data Availability Statement

VIIRS Moderate Resolution 6-Min L1B Swath 750m and Moderate Resolution Terrain-Corrected Geolocation 6-Min L1 Swath 750m were acquired from the Level-1 and Atmosphere Archive & Distribution System (LAADS) Distributed Active Archive Center (DAAC), located in the Goddard Space Flight Center in Greenbelt, Maryland [27–32]. The Non Time Critical Sentinel-3 SLSTR Level-1b data and the Sentinel-5P Precursor Level 2 Methane data were downloaded from [dataspace.copernicus.eu](https://dataspace.copernicus.eu). ERA5 wind data was downloaded from the Copernicus Climate Change Service [24]. The data was analyzed using Python, making extensive use of the NumPy [33], SciPy [34], xarray [35, 36] and matplotlib [37, 38] libraries.

## Acknowledgements

We thank Andrea Sanchez Mediavilla for her contribution on the Sentinel-3 related parts of the work and Mathieu Dogniaux for help on the water spectrum continuum. This research has been funded in the framework of UNEP’s International Methane Emissions Observatory (IMEO).

## References

- [1] Ilissa B. Ocko et al. “Acting rapidly to deploy readily available methane mitigation measures by sector can immediately slow global warming”. In: *Environmental Research Letters* 16.5 (May 2021). Publisher: IOP Publishing, p. 054042. ISSN: 1748-9326. DOI: 10.1088/1748-9326/abf9c8. URL: <https://dx.doi.org/10.1088/1748-9326/abf9c8>.
- [2] T. Lauvaux et al. “Global assessment of oil and gas methane ultra-emitters”. In: *Science* 375.6580 (Feb. 4, 2022), pp. 557–561. ISSN: 0036-8075, 1095-9203. DOI: 10.1126/science.abj4351. URL: <https://www.science.org/doi/10.1126/science.abj4351>.
- [3] Daniel Zavala-Araiza et al. “Toward a Functional Definition of Methane Super-Emitters: Application to Natural Gas Production Sites”. In: *Environmental Science & Technology* 49.13 (2015). PMID: 26148555, pp. 8167–8174. DOI: 10.1021/acs.est.5b00133. eprint: <https://doi.org/10.1021/acs.est.5b00133>. URL: <https://doi.org/10.1021/acs.est.5b00133>.
- [4] J. P. Veefkind et al. “TROPOMI on the ESA Sentinel-5 Precursor: A GMES mission for global observations of the atmospheric composition for climate, air quality and ozone layer applications”. In: *Remote Sensing of Environment*. The Sentinel Missions - New Opportunities for Science 120 (May 15, 2012), pp. 70–83. ISSN: 0034-4257. DOI: 10.1016/j.rse.2011.09.027. URL: <https://www.sciencedirect.com/science/article/pii/S0034425712000661>.
- [5] A. Lorente et al. “Accounting for surface reflectance spectral features in TROPOMI methane retrievals”. In: *Atmospheric Measurement Techniques* 16.6 (2023), pp. 1597–1608. DOI: 10.5194/amt-16-1597-2023. URL: <https://amt.copernicus.org/articles/16/1597/2023/>.
- [6] Daniel J. Jacob et al. “Quantifying methane emissions from the global scale down to point sources using satellite observations of atmospheric methane”. In: *Atmospheric Chemistry and Physics* 22.14 (July 29, 2022), pp. 9617–9646. ISSN: 1680-7324. DOI: 10.5194/acp-22-9617-2022. URL: <https://acp.copernicus.org/articles/22/9617/2022/>.

- [7] Daniel J. Varon et al. “High-frequency monitoring of anomalous methane point sources with multispectral Sentinel-2 satellite observations”. In: *Atmospheric Measurement Techniques* 14.4 (Apr. 12, 2021). Publisher: Copernicus GmbH, pp. 2771–2785. ISSN: 1867-1381. DOI: 10.5194/amt-14-2771-2021. URL: <https://amt.copernicus.org/articles/14/2771/2021/>.
- [8] Thibaud Ehret et al. “Global Tracking and Quantification of Oil and Gas Methane Emissions from Recurrent Sentinel-2 Imagery”. In: *Environmental Science & Technology* 56.14 (July 19, 2022). Publisher: American Chemical Society, pp. 10517–10529. ISSN: 0013-936X. DOI: 10.1021/acs.est.1c08575. URL: <https://doi.org/10.1021/acs.est.1c08575>.
- [9] Sudhanshu Pandey et al. “Daily detection and quantification of methane leaks using Sentinel-3: a tiered satellite observation approach with Sentinel-2 and Sentinel-5p”. In: *Remote Sensing of Environment* 296 (Oct. 1, 2023), p. 113716. ISSN: 0034-4257. DOI: 10.1016/j.rse.2023.113716. URL: <https://www.sciencedirect.com/science/article/pii/S0034425723002675>.
- [10] Berend J. Schuit et al. “Automated detection and monitoring of methane super-emitters using satellite data”. In: *Atmospheric Chemistry and Physics* 23.16 (Sept. 19, 2023). Publisher: Copernicus GmbH, pp. 9071–9098. ISSN: 1680-7316. DOI: 10.5194/acp-23-9071-2023. URL: <https://acp.copernicus.org/articles/23/9071/2023/>.
- [11] E. Polehampton et al. *Copernicus Sentinel-3 SLSTR Land User Handbook, Section 8.2.13*. 2023. URL: <https://sentinel.esa.int/documents/247904/4598082/Sentinel-3-SLSTR-Land-Handbook.pdf>.
- [12] Jean-Louis Roujean, Marc Leroy, and Pierre-Yves Deschamps. “A bidirectional reflectance model of the Earth’s surface for the correction of remote sensing data”. In: *Journal of Geophysical Research* 97 (D18 1992), p. 20455. ISSN: 0148-0227. DOI: 10.1029/92JD01411. URL: <http://doi.wiley.com/10.1029/92JD01411>.
- [13] Yan Liu et al. “Evaluation of the VIIRS BRDF, Albedo and NBAR products suite and an assessment of continuity with the long term MODIS record”. In: *Remote Sensing of Environment* 201 (Nov. 1, 2017), pp. 256–274. ISSN: 0034-4257. DOI: 10.1016/j.rse.2017.09.020. URL: <https://www.sciencedirect.com/science/article/pii/S0034425717304339>.
- [14] Sudhanshu Pandey et al. “Satellite observations reveal extreme methane leakage from a natural gas well blowout”. In: *Proceedings of the National Academy of Sciences* 116.52 (Dec. 26, 2019). Company: National Academy of Sciences Distributor: National Academy of Sciences Institution: National Academy of Sciences Label: National Academy of Sciences Publisher: Proceedings of the National Academy of Sciences, pp. 26376–26381. DOI: 10.1073/pnas.1908712116. URL: <https://www.pnas.org/doi/abs/10.1073/pnas.1908712116>.
- [15] Marc Watine-Guiu et al. “Geostationary satellite observations of extreme and transient methane emissions from oil and gas infrastructure”. In: *Proceedings of the National Academy of Sciences* 120.52 (Dec. 26, 2023). Publisher: Proceedings of the National Academy of Sciences, e2310797120. DOI: 10.1073/pnas.2310797120. URL: <https://www.pnas.org/doi/10.1073/pnas.2310797120>.
- [16] G P Anderson et al. “AFGL Atmospheric Constituent Profiles (0-120km)”. In: *Tech. Rep. AFGL-TR-86-0110* (1986).
- [17] *Climate Change Indicators: Atmospheric Concentrations of Greenhouse Gases*. <https://www.epa.gov/climate-indicators/climate-change-indicators-atmospheric-concentrations-greenhouse-gases>. Accessed: 2023-12-22.
- [18] *Copernicus Climate indicators*. <https://climate.copernicus.eu/climate-indicators>. Accessed: 2023-12-22.

- [19] Keith P. Shine et al. “The water vapour continuum in near-infrared windows – Current understanding and prospects for its inclusion in spectroscopic databases”. In: *Journal of Molecular Spectroscopy*. New Visions of Spectroscopic Databases, Volume II 327 (Sept. 1, 2016), pp. 193–208. ISSN: 0022-2852. DOI: 10.1016/j.jms.2016.04.011. URL: <https://www.sciencedirect.com/science/article/pii/S0022285216300637>.
- [20] Esri and Maxar. *Esri World Imagery*. dataset. 2021. URL: [https://services.arcgisonline.com/ArcGIS/rest/services/World\\_Imagery/MapServer](https://services.arcgisonline.com/ArcGIS/rest/services/World_Imagery/MapServer).
- [21] Mahesh Kumar Sha et al. “Validation of methane and carbon monoxide from Sentinel-5 Precursor using TCCON and NDACC-IRWG stations”. In: *Atmospheric Measurement Techniques* 14.9 (Sept. 28, 2021). Publisher: Copernicus GmbH, pp. 6249–6304. ISSN: 1867-1381. DOI: 10.5194/amt-14-6249-2021. URL: <https://amt.copernicus.org/articles/14/6249/2021/>.
- [22] Jürgen Fisher. *Retrieval of total water vapour content from OLCI measurements*. Technical Document. Sentinel-3 OLCI Water Vapour ATBD. Sept. 20, 2012. URL: [https://sentinels.copernicus.eu/web/sentinel/user-guides/sentinel-3-olci/document-library/-/asset\\_publisher/hkf7sg9Ny1d5/content/id/637522](https://sentinels.copernicus.eu/web/sentinel/user-guides/sentinel-3-olci/document-library/-/asset_publisher/hkf7sg9Ny1d5/content/id/637522).
- [23] Google. *Google Maps Map Tiles*. dataset. 2024.
- [24] H. Hersbach et al. *ERA5 hourly data on single levels from 1940 to present*. dataset. 2023. DOI: 10.24381/cds.adbb2d47.
- [25] Associated Press News. *Idaho officials order brief evacuation of about 10,000 people after reported gas pipeline explosion*. <https://apnews.com/article/gas-line-explosion-idaho-town-evacuated-47c4c5df577ed0e6d52245eb6d084b96>. Accessed: 2023-12-22. 2023.
- [26] Oswald Wallner, Thido Reinert, and Christoph Straif. “METIMAGE: a spectro-radiometer for the VII mission onboard METOP-SG”. In: *International Conference on Space Optics — ICSO 2016*. International Conference on Space Optics — ICSO 2016. Vol. 10562. SPIE, Sept. 25, 2017, pp. 107–114. DOI: 10.1117/12.2296103. URL: <https://www.spiedigitallibrary.org/conference-proceedings-of-spie/10562/105620E/METIMAGE--a-spectro-radiometer-for-the-VII-mission-onboard/10.1117/12.2296103.full>.
- [27] VIIRS Calibration Support Team (VCST). *VIIRS/NPP Moderate Resolution Bands L1B 6-Min Swath 750m*. dataset. 2021. DOI: 10.5067/VIIRS/VNP02MOD.002. URL: <https://ladsweb.modaps.eosdis.nasa.gov/missions-and-measurements/products/VNP02MOD/>.
- [28] VIIRS Calibration Support Team (VCST). *VIIRS/JPSS1 Moderate Resolution Bands L1B 6-Min Swath 750m*. dataset. 2021. DOI: 10.5067/VIIRS/VJ102MOD.021. URL: <https://ladsweb.modaps.eosdis.nasa.gov/missions-and-measurements/products/VJ102MOD/>.
- [29] VIIRS Calibration Support Team (VCST). *VIIRS/JPSS2 Moderate Resolution Bands L1B 6-Min Swath 750 m*. dataset. 2023. DOI: 10.5067/VIIRS/VJ202MOD.002. URL: <https://ladsweb.modaps.eosdis.nasa.gov/missions-and-measurements/products/VJ202MOD/>.
- [30] VIIRS Calibration Support Team (VCST). *VIIRS/NPP Moderate Resolution Terrain-Corrected Geolocation L1 6-Min Swath- 750m*. dataset. 2021. DOI: 10.5067/VIIRS/VNP03MOD.002. URL: <https://ladsweb.modaps.eosdis.nasa.gov/missions-and-measurements/products/VNP03MOD/>.
- [31] VIIRS Calibration Support Team (VCST). *VIIRS/JPSS1 Moderate Resolution Terrain-Corrected Geolocation L1 6-Min Swath- 750m*. dataset. 2021. DOI: 10.5067/VIIRS/VJ103MOD.021. URL: <https://ladsweb.modaps.eosdis.nasa.gov/missions-and-measurements/products/VJ103MOD/>.

- [32] VIIRS Calibration Support Team (VCST). *VIIRS/JPSS2 Moderate Resolution Terrain-Corrected Geolocation L1 6-Min Swath 750 m.* dataset. 2023. DOI: 10.5067/VIIRS/VJ203MOD.002. URL: <https://ladsweb.modaps.eosdis.nasa.gov/missions-and-measurements/products/VJ203MOD/>.
- [33] Charles R. Harris et al. “Array programming with NumPy”. In: *Nature* 585.7825 (Sept. 2020), pp. 357–362. DOI: 10.1038/s41586-020-2649-2. URL: <https://doi.org/10.1038/s41586-020-2649-2>.
- [34] Pauli Virtanen et al. “SciPy 1.0: Fundamental Algorithms for Scientific Computing in Python”. In: *Nature Methods* 17 (2020), pp. 261–272. DOI: 10.1038/s41592-019-0686-2.
- [35] S. Hoyer and J. Hamman. “xarray: N-D labeled arrays and datasets in Python”. In: *Journal of Open Research Software* 5.1 (2017). DOI: 10.5334/jors.148. URL: <https://doi.org/10.5334/jors.148>.
- [36] Stephan Hoyer et al. *xarray*. software library. 2022. DOI: 10.5281/ZENODO.7392365. URL: <https://zenodo.org/record/7392365>.
- [37] J. D. Hunter. “Matplotlib: A 2D graphics environment”. In: *Computing in Science & Engineering* 9.3 (2007), pp. 90–95. DOI: 10.1109/MCSE.2007.55.
- [38] The Matplotlib Development Team. *Matplotlib: Visualization with Python*. software library. 2023. DOI: 10.5281/ZENODO.10150955. URL: <https://zenodo.org/doi/10.5281/zenodo.10150955>.

# Supporting Information for “Daily global methane super-emitter detection and source identification with sub-daily tracking”

## Spectral Response

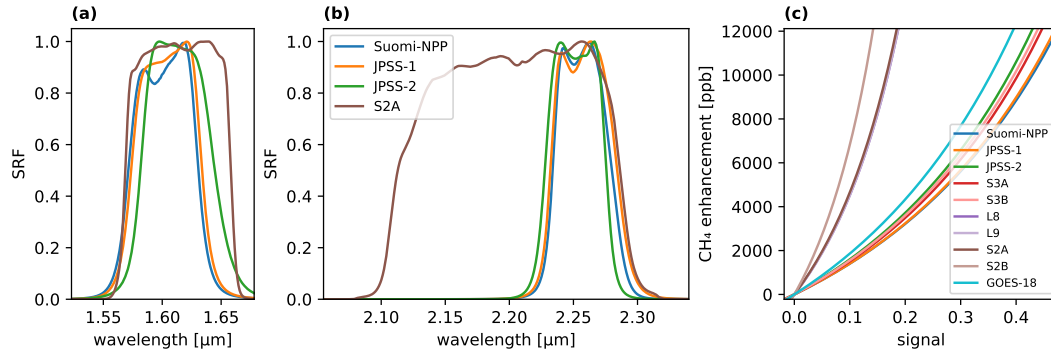


Figure S1: (a,b) Spectral response functions (SRF) of the JPSS satellites in the 1.6 μm and 2.2 μm SWIR bands. For comparison, the Sentinel-2A sensitivity is also shown. (c) Methane sensitivity of the signal for JPSS, Sentinel-2/3, Landsat and GOES-18 instruments, assuming an air mass factor of 3.5. Suomi-NPP and JPSS-1 are the most sensitive, Sentinel-2B the least sensitive to methane.

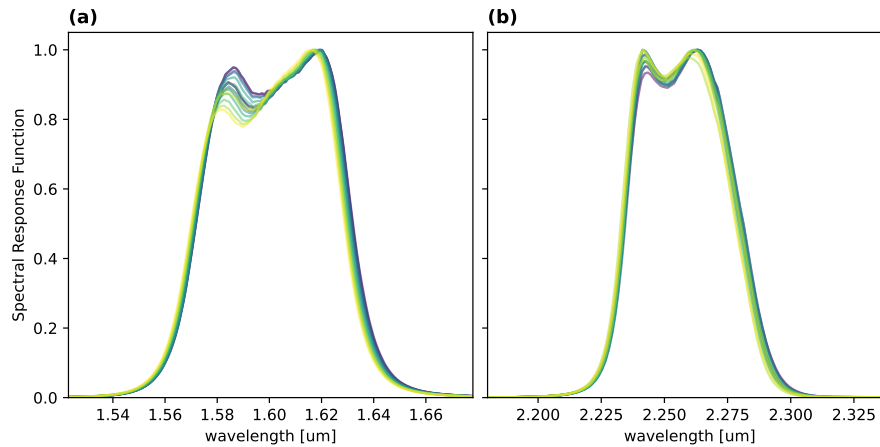


Figure S2: Individual detector Spectral response functions of M10 and M11 band detectors in panel (a) and (b) respectively, for the Suomi-NPP VIIRS instrument, as measured before launch. Taken from <https://ncc.nesdis.noaa.gov/VIIRS/VIIRSSpectralResponseFunctions.php>.

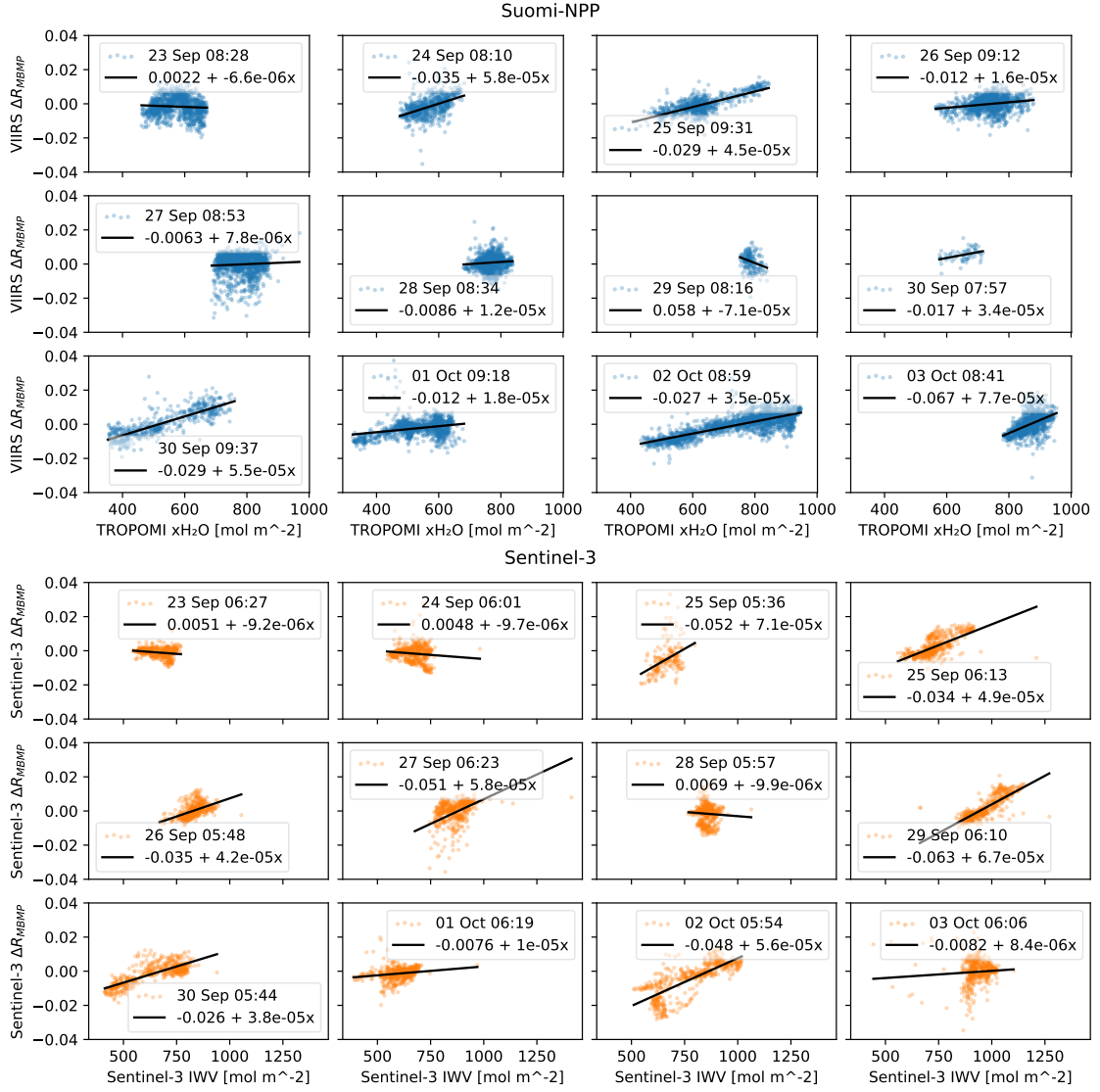


Figure S3: (top) Correlation between Suomi-NPP VIIRS  $\Delta R_{MBMP}$  and the co-located TROPOMI  $xH_2O$  total water column of overpasses over the Malay area for the period 23 September to 3 October 2023, using all data of the scene resampled to TROPOMI pixels. (bottom) Correlation between Sentinel-3  $\Delta R_{MBMP}$  and Sentinel-3 Integrated Water Vapor of the same days and area.

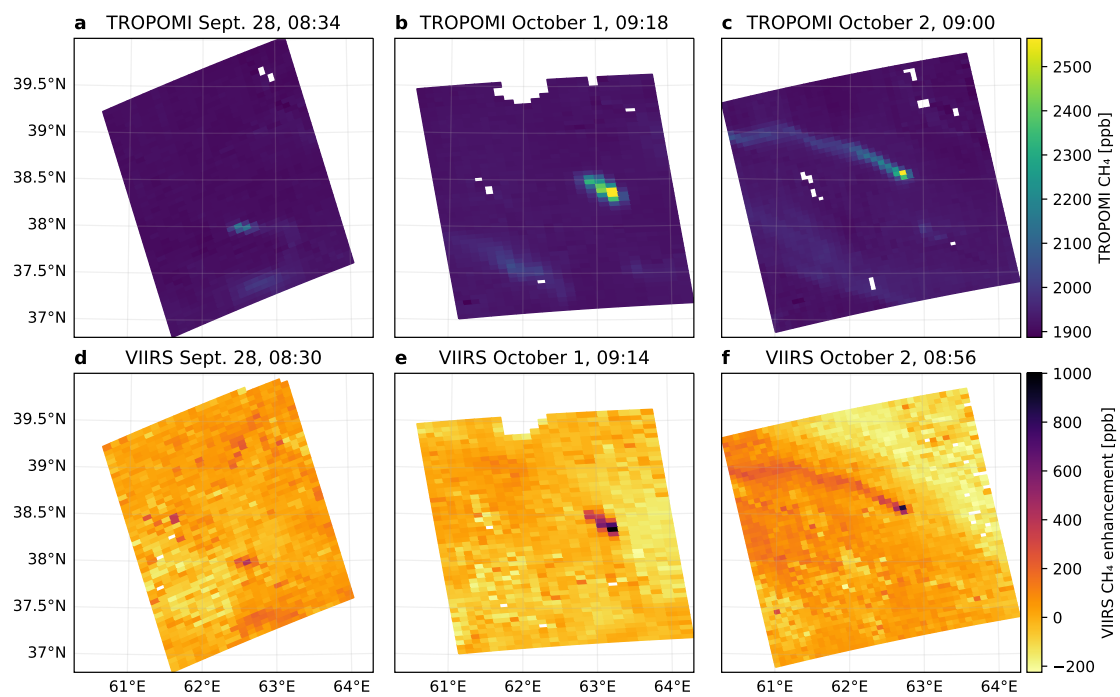


Figure S4: Comparison between resampled TROPOMI data and VIIRS data. (a-c) TROPOMI data of methane plumes in Eastern Turkmenistan on September 28, October 1 and October 2 respectively. (d-f) Co-located VIIRS MBMP, resampled to the corresponding TROPOMI pixels. This figure corresponds to the plots in Figure 2(m-o). (d) corresponds to Figure S9(t), (e) corresponds to Figure 2(d), (f) corresponds to Figure 2(i).

## Time series of emission events.

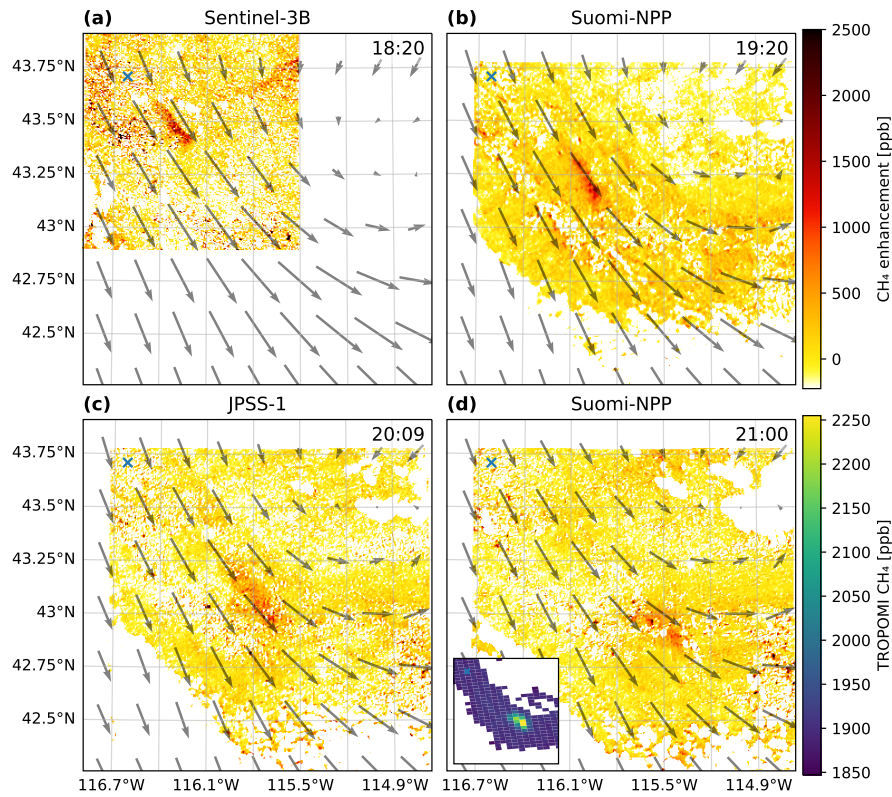


Figure S5: Methane enhancements from VIIRS and Sentinel-3 for the pipeline leak near Middleton, Idaho on October 12th 2023. Arrows indicate ERA5 100m wind, blue cross marks Middleton, where an excavator ruptured a natural gas pipeline [25]. Panel (b) corresponds to Figure 4(a). Note: No TROPOMI data is available for the overpass in (b), as it was covered by the edge of VIIRS swath. The only TROPOMI data for this event is the data shown in the inset of (d).

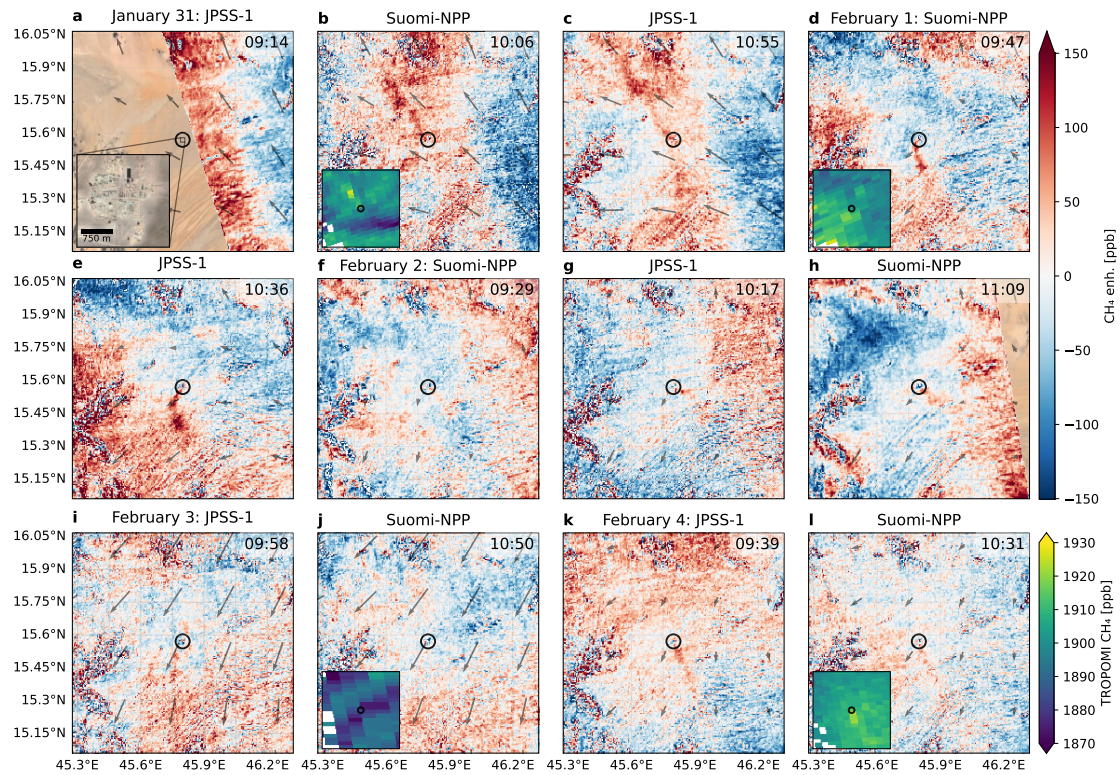


Figure S6: VIIRS monitoring of methane emissions from an oil/gas facility in Yemen, located at  $15.56^{\circ}\text{N}$ ,  $45.79^{\circ}\text{E}$  (centre of the field of view, circled in black). Shown are the VIIRS overpasses between January 31 and February 4, 2023, and the corresponding TROPOMI overpasses. Field of view of the TROPOMI insets corresponds to the field of view of the VIIRS panels. No TROPOMI data are available for the overpasses in (f,h). Although there is large-scale water vapor concentration variation, causing large areas of apparent positive and negative enhancement, this represents an almost ideal case, with plumes consisting of methane enhancements smaller than 150ppb visible. Panel (e) corresponds to Figure 4(g). Background imagery and inset of (a) are Google maps imagery [23].

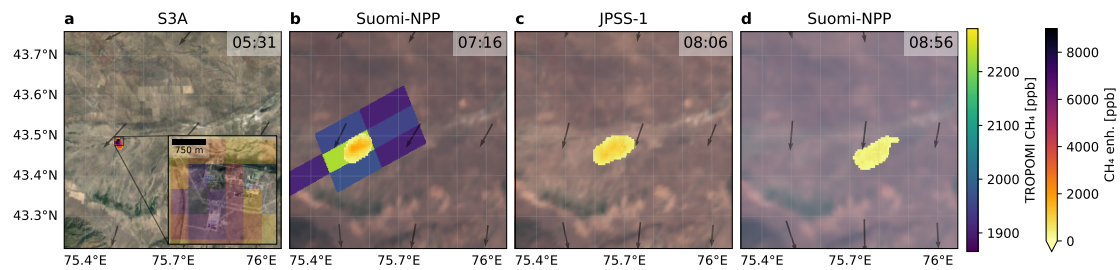


Figure S7: Emission from a gas compressor station in East-Kazakhstan, located at  $43.49^{\circ}\text{N}$ ,  $75.51^{\circ}\text{E}$  (Inset of (a)). The emission started before the Sentinel-3 overpass in (a), but ended before the overpass of Suomi-NPP and Sentinel-5P in panel (b). Background of panel (a) is Google Maps imagery [23], of panel (b-d) the corresponding VIIRS RGB data. Panel(b) corresponds to Figure 4(c)

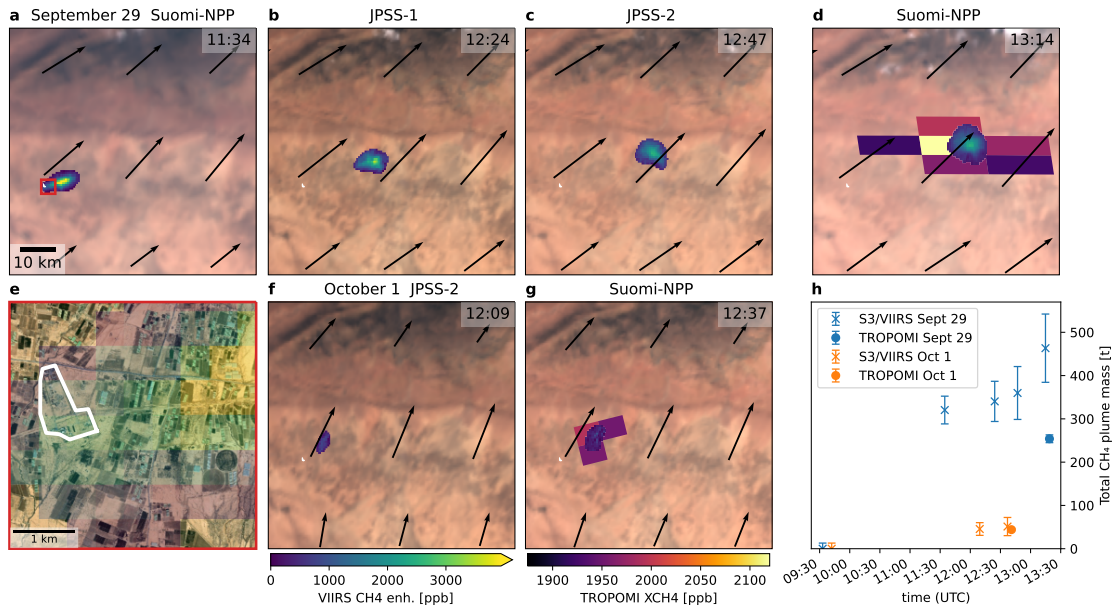


Figure S8: Methane releases at a compressor station at  $34.676^{\circ}\text{N}$ ,  $6.191^{\circ}\text{E}$  in Algeria (marked in white) as observed by the various VIIRS instruments on Suomi-NPP, JPSS-1 and JPSS-2 on 29th Sept and 1 Oct 2023. For the Suomi-NPP VIIRS observation (d, g) we also show the TROPOMI observation, no TROPOMI observation is available for panel (a), as the location falls outside the TROPOMI swath. In (e), we show the plume in (a) over the facility, outlined in white. The extent of (e) is indicated by the red box in (a). Background images are level-1b VIIRS RGB-images of the respective overpasses, except for zoombox (e), which uses ESRI world imagery [20]. No plumes were observed in the Sentinel-3 overpasses of 9:33UTC on September 29th and 9:42UTC of October first. (h) Total methane in the plume as a function of time. Panel (a,d) correspond to Figure 4(h-i). The clear separation of the plume from the source enables cross-verification between the different observations, as the amount of methane in the plume should remain constant. For the last overpass of the 29th, the amount of methane in the plume is somewhat larger. Inspection of the full methane field shows that this is due to a non-local enhancement in the MBMP, probably due to water vapor. Comparing the VIIRS and TROPOMI based emission estimates we again see the TROPOMI estimates are significantly lower. However, retrieval of adjacent TROPOMI-pixels failed due to altitude roughness, which can explain some of the difference as we might be missing some of the methane plume mass in the TROPOMI observation. Part of the difference could also be due to the partial pixel enhancement effect.



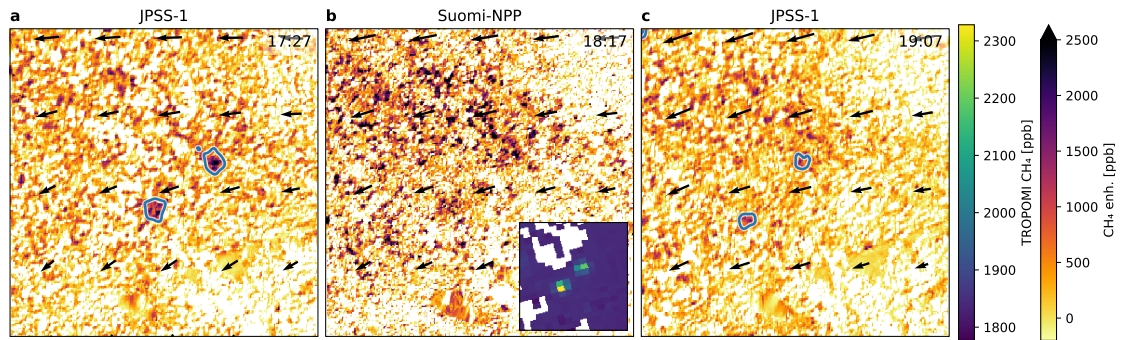


Figure S10: VIIRS observations of two methane blobs over agricultural land in Argentina. Blue outlines in (a,c) indicate  $\sigma = 1.2$  level outlier plume detection using MAD as described in the main text. Inset in (b) shows data of the corresponding TROPOMI overpass. Panel (a) corresponds to the overpass also shown in Figure 4(e) of the main text.

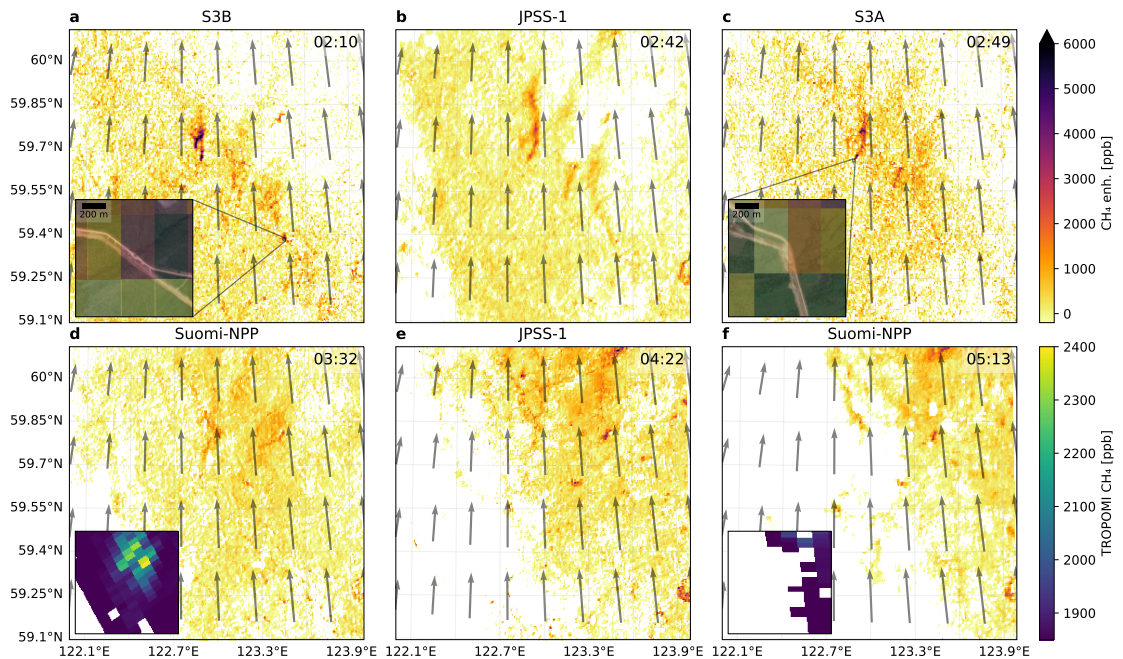


Figure S11: VIIRS and Sentinel-3 observations of methane plumes vented from the 'Power of Siberia' pipeline in Eastern Russia observed on September 22, 2021. Multiple, simultaneously emitting sources can be observed, leading to a complex plume structure in TROPOMI (inset (d)). Background of insets (a,c) is ESRI world imagery [20]. Black arrows correspond to 100m ERA5 wind, scaled to represent 1 hour travel time. Panel (b) corresponds to the overpass also shown in Figure 4(d) of the main text.

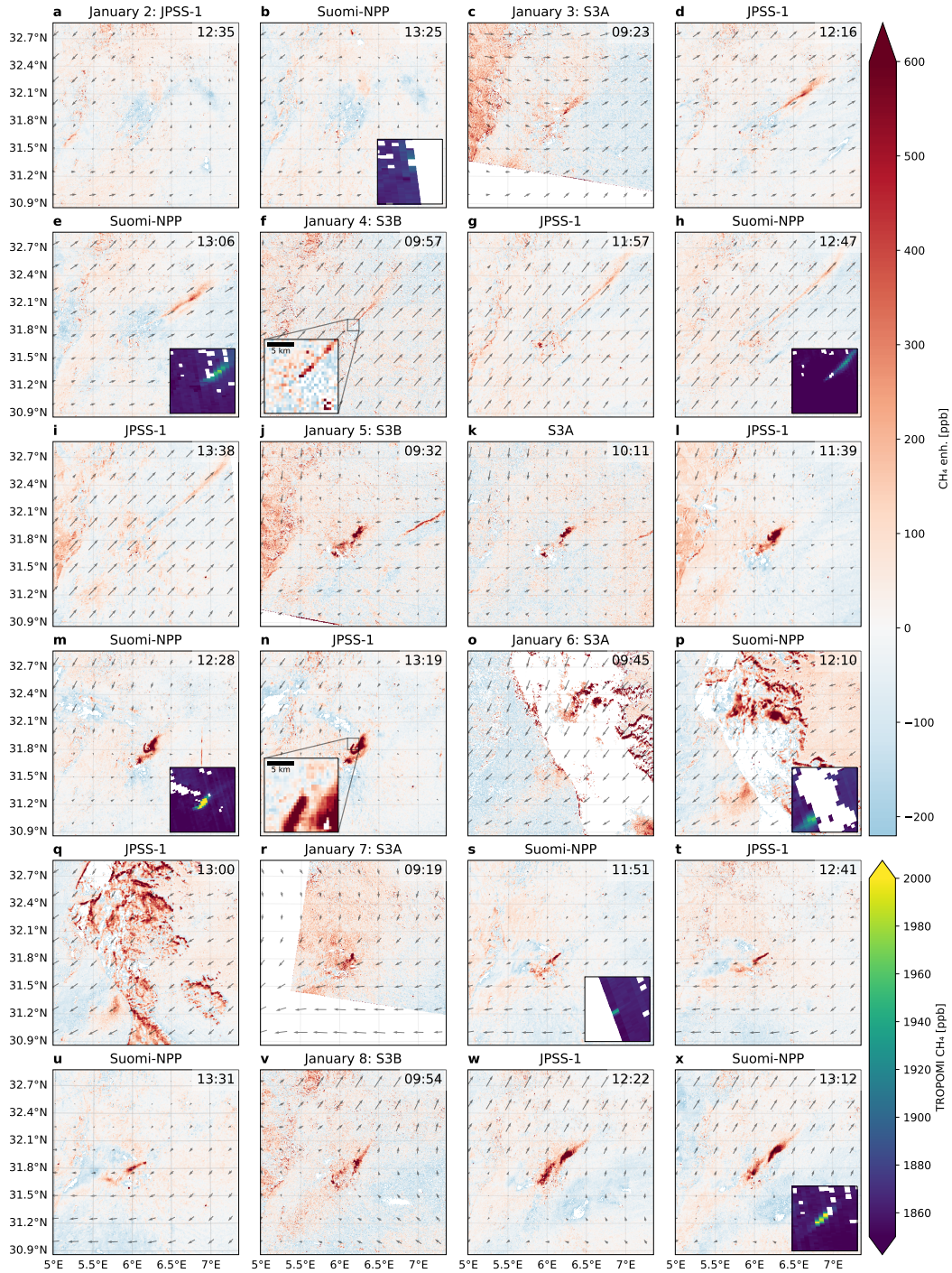


Figure S12: Retrieved VIIRS and Sentinel-3 data for the Hassi Messaoud event in 2020, which started on January 3rd 2020. (source in centre of the field of view). We chose this example as it has been well-studied using other satellites [6, 7, 9] and it represents favorable observation conditions as it is in a desert area. This event lasted for 6 days. During this period, 6 clear-sky overpasses of TROPOMI, 1 overpass of Sentinel-2 satellites, 6 overpasses of Sentinel-3 satellites and 14 overpasses of Suomi-NPP and JPSS-1, the two active VIIRS platforms at the time, occurred. Insets in (b,e,h,m,p,s,x) show data from corresponding TROPOMI overpasses. On the 6th of January (panels o-q) weather conditions were cloudy. ERA5 100m winds are plotted as arrows in each subplot. (w) corresponds to Figure 4.